JGR Space Physics

RESEARCH ARTICLE
10.1029/2020JA028122

# Relationship Between Presunset Wave Structures and Interbubble Spacing: The Seeding Perspective of Equatorial Plasma Bubble

S. K. Das[1], A. K. Patra[1], E. A. Kherani[2], P. Pavan Chaitanya[1], and K. Niranjan[3]

[1]National Atmospheric Research Laboratory, Gadanki, India, [2]Instituto Nacional de Pesquisas Espaciais, São José dos Campos, Brazil, [3]Department of Physics, Andhra University, Visakhapatnam, India

**Key Points:**
- Simultaneous observations of horizontal wavelength of ionospheric wave-like structures and interbubble spacing are presented
- Good relationship between the horizontal wavelength and interbubble spacing has been found
- Potential of digisonde observations providing one of the precursors of EPB is demonstrated

**Correspondence to:**
A. K. Patra,
akpatra@narl.gov.in

**Citation:**
Das, S. K., Patra, A. K., Kherani, E. A., Chaitanya, P. P., & Niranjan, K. (2020). Relationship between presunset wave structures and interbubble spacing: The seeding perspective of equatorial plasma bubble. *Journal of Geophysical Research: Space Physics*, *125*, e2020JA028122. https://doi.org/10.1029/2020JA028122

Received 16 APR 2020
Accepted 24 JUN 2020
Accepted article online 15 JUL 2020

**Abstract** In this paper, we study on the precursor seed structures well before the prospective occurrence of equatorial plasma bubble (EPB). We use the scanning mode observations made by the 30-MHz Gadanki Ionospheric Radar Interferometer for estimating interbubble spacing and high time resolution observations made by a collocated digisonde for inferring horizontal wavelength of wave-like variations prior to the onset of EPB. Horizontal wavelength of wave-like variations has been inferred from plasma density variations and height variations of isodensity contours; both show consistent results. Remarkable agreement has been found between the estimated horizontal wavelength and interbubble spacing, which demonstrates the potential of digisonde in providing relevant seed structure for a prospective EPB formation. Further analysis based on observational results and numerical simulation of collisional interchange instability shows that while the eventual formation of EPB has a strong bearing on the height of the *F* layer and density gradient scale length, the growth perspective of the EPB depends on the seed wavelength. These results are presented and discussed keeping the future prospective of EPB forecasting/nowcasting.

## 1. Introduction

Equatorial plasma bubble (EPB) and associated plasma irregularities continue to be topics of research in the scientific community due to their detrimental effects on satellite-based navigation and communication systems, high-frequency communication, and over-the-horizon radar applications. Although we have a fairly good understanding on the genesis of EPB, the day-to-day variability of EPB still remains poorly understood, implying that forecasting the occurrence of EPB on a given night remains a challenge.

As per the current understanding, EPB is a manifestation of the Rayleigh-Taylor (RT) instability initiated at the postsunset bottomside *F* region where the electron density gradient is upward and antiparallel to gravity. The growth of the instability, however, depends on various background conditions including the height of the *F* layer, spatial gradient in electron density, and zonal electric field. Observationally, it has been found that the occurrence of EPB statistically correlates well with the prereversal enhancement of zonal electric field (e.g., Kil et al., 2009; Su et al., 2008). This is understandable considering that large zonal electric field lifts the *F* region to higher up where ion-neutral collision frequency is low, which enhances the growth of the RT instability. The prereversal enhancement of zonal electric field alone, however, has not proven to be sufficient enough for the development of a reliable forecasting capability for the occurrence/nonoccurrence of EPB (e.g., Huang & Hairston, 2015; Smith et al., 2016).

Given that the growth of the RT instability would take several hundreds to thousands of seconds if it were to grow from background noise like fluctuations (e.g., Huang & Kelley, 1996b; Kelley, 1985), seed structure has been invoked as an important prerequisite to overcome the otherwise slow growth rate of the RT instability. The fact that fully developed EPBs have been observed after a few minutes of the sunset supports the notion of the seeding hypothesis of EPB. In fact, ALTAIR incoherent scatter radar observations revealed wave structures prior to the occurrence of EPB supporting the seeding hypothesis (Hysell & Kudeki, 2004; Tsunoda, 1983; Tsunoda & White, 1981). Observations also revealed that zonal dimension of EPB and interbubble spacing, which are typically in the range of 200–500 km, could vary remarkably from one night to the other even for similar background ionospheric conditions. Considering the importance and variability of seed structures in EPB development, atmospheric gravity waves have been repeatedly invoked as a possible source of spatial structuring capable of seeding the EPB (e.g., Fukao et al., 2006; Huang & Kelley, 1996a,

1996b; Hysell & Chau, 2006; Hysell et al., 1990; Kelley et al., 1981; Makela et al., 2010; Röttger, 1973; Singh et al., 1997; Sreeja et al., 2009; Takahashi et al., 2009; Taori et al., 2011; Tsunoda & White, 1981). It may, however, be kept in mind that there are experimental difficulties in obtaining gravity waves parameters in the neutral medium at the *F* region (e.g., Kudeki et al., 2007). Accordingly, gravity wave-like variations in plasma parameters have been used as proxy to study the seeding in question (e.g., Abdu et al., 2009; Kelley et al., 1981; Narayanan et al., 2012; Patra et al., 2013; Sreeja et al., 2009; Taori et al., 2011). Conspicuously, a few studies have used temporal variation of the *F* layer height observed by a digisonde to infer gravity wave-associated perturbations as possible structures seeding the EPB and demonstrated the potential applications of such observations as precursor for EPB forecasting (e.g., Abdu et al., 2009, 2015). Motivated by these studies, we have examined digisonde observations in an effort to test the potential and reliability of such observations providing the seed/precursor for EPB development.

In this paper, we present a detailed analysis on the above aspects using collocated observations made using the scanning capability of the 30 MHz Gadanki Ionospheric Radar Interferometer (GIRI) and a DPS-4D digisonde from Gadanki (13.5°N, 79.2°E, 6.5°N magnetic latitude). Notably, we use the scanning capability of the GIRI to obtain spatial structures of EPB so that the inferred spatial scales from gravity wave-like variations in digisonde observations can be correlated with them. While the results show very good agreement between the two parameters, implying that the gravity wave-like variations observed by digisonde can be considered as one of the precursors of EPB, background ionosphereic parameters prevailing during the sunset are crucial. We find that by taking into account the background ionospheric conditions, namely, density gradient, height of the *F* layer, and vertical plasma drift, reasonable success can be achieved.

## 2. Observations and Data Analysis

Results presented here were based on collocated observations made using the 30-MHz GIRI and a DPS-4D digisonde from Gadanki. We used the scanning capability of the GIRI to study east-west distribution of field-aligned irregularities associated with radar plumes representing the EPBs (Patra et al., 2014). Importantly, the scanning capability of the GIRI allowed us to study east-west structures and drifts of EPBs. For the present investigation, we have examined 125 nights of observations made during 2015–2016. Out of these nights, the EPBs occurred on 49 nights.

GIRI observations were made in scanning mode, using 17 azimuthal beam positions at a step of 5° within azimuth angle of ±40°, as shown in Figure 1a. Each scan cycle, consisting of 17 beam observations, took 50 s. Figure 1b shows range-time variations of signal-to-noise-ratio (SNR) corresponding to nine beam positions observed on 26 March 2015. The maps are shown at 10° step to bring clarity in the structures: the top panel illustrating the observations made with the west-40° beam and the bottom panel illustrating observations made with the east-40° beam. The slant solid lines indicate the eastward progression of a bubble, and the vertical dashed line indicates the east-west spacing between two bubbles. Note that the second bubble appeared at the west-40° beam when the first bubble was about to exit the east-40° beam. In order to estimate the interbubble spacing in the east-west plane, we show spatial distribution of echo SNR at 350 km in range as a function of time in Figure 1c. Vertical axis represents zonal distance mapped from azimuth angles corresponding to the height under consideration, and positive (negative) value represents eastward (westward) distance from Gadanki. Dashed lines represent eastward progression, and thick dashed line intersecting the slant lines represents interbubble spacing. The interbubble spacing is estimated to be 450 km. Also note that the structures progressed eastward irrespective of their first sighting at any location in the zonal plane and the average eastward drift of the echoing regions (plumes) in this case is estimated to be 125 m $s^{-1}$.

Digisonde observations were made at 5-min interval. For studying wave-like variations in electron density, we have scaled ionograms to obtain variations in the virtual height of the *F* layer ($h'F$) from plasma frequency reflection at plasma frequency of 5, 6, and 7 MHz and electron density variations at 330, 360, and 390 km. Vertical drift velocities ($V_z$) have been estimated by averaging $d(h'F)/dt$ observed at the three frequencies. It may be mentioned that the $V_z$ values of concern here are those corresponding to the evening time when convection dominates other processes and the digisonde-based $V_z$ values are good representation of the vertical plasma drifts (Woodman et al., 2006). For characterizing the gravity wave-like variations, the

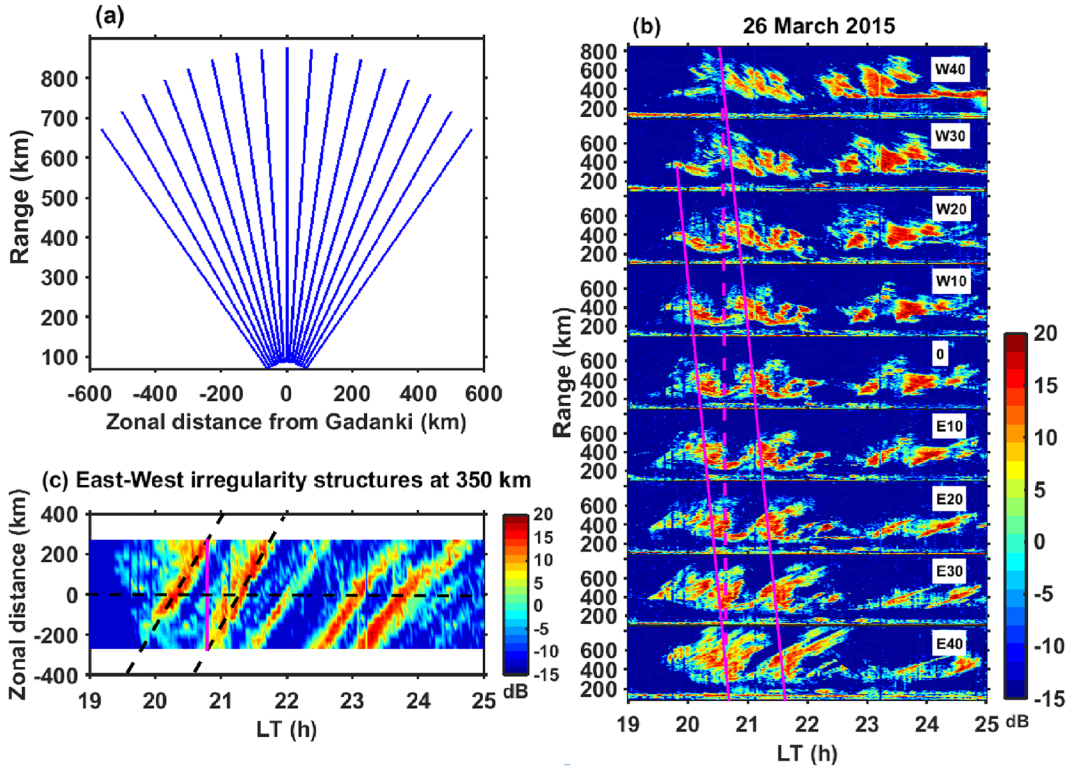


**Figure 1.** (a) GIRI 17-beam positions used for scanning mode observations; (b) range-time SNR maps of the radar echoes observed in nine beam positions, each separated by 10°, on 26 March 2015. The slant solid lines represent eastward progression of bubble, and the vertical dashed line indicates the east-west spacing between two bubbles. (c) Zonal distribution of irregularities at 350 km presented in terms of echo SNR. Magenta thick line intersecting the slant dashed lines represents interbubble spacing.

residuals, obtained by subtracting the mean height variations (30-min running average) from the actual height variations, are band-passed with a period of 20–90 min. Similar exercise was done for electron density also. The horizontal wavelength of gravity wave-like variations at the bottom side of the *F* layer, which is of interest here, is obtained as follows. First, the vertical wavelength of the gravity wave-like variations is obtained using the plane wave approximation as

$$\lambda_v = \frac{\Delta h}{\Delta t} T, \tag{1}$$

where $\lambda_v$ is the vertical wavelength, $T$ is the wave period, and $\Delta h$ and $\Delta t$ are the height and time intervals in which the downward phase of the wave-like variations is maintained. After estimating the vertical wavelength ($\lambda_v$), the horizontal wavelength ($\lambda_x$) is obtained using the dispersion relation of gravity wave. We, however, have assumed the background wind to be zero, which is not realistic. The fact that we do not have concurrent measurement of wind, we have taken this approach. We, however, will discuss this aspect while presenting and comparing the estimated horizontal wavelength with the interbubble spacing. For the present purpose, the horizontal wavelength is estimated as (Fritts & Alexander, 2003)

$$\lambda_x = 2\pi \frac{\sqrt{(T^2/{T_b}^2 - 1)}}{\sqrt{(1/{\lambda_v}^2 + 1/16\pi^2 H^2)}}, \tag{2}$$

where $\lambda_x$ is the horizontal wavelength of the gravity wave-like variations, $T_b$ is the Brunt Vaisala period, and $H$ is the scale height at 300 km. In the present case, $T_b$ and $H$ are taken as 15 min and 50 km, respectively.

## 3. Observational Results

### 3.1. Formation of EPB With Linkage to Wave-Like Variations

Figures 2a–2d show the results of digisonde observations, illustrating temporal variations of the virtual height of the botomside $F$ region ($h'F$), vertical plasma drift ($V_z$), residual electron density (d$N_e$), and residual virtual height (d$h'F$), respectively, observed on 20 March 2015. Height variations/perturbations observed at 5, 6, and 7 MHz (Figures 2a and 2d) and electron density perturbations at 330, 360, and 390 km (Figure 2c) are shown in different colors. Also, values of d$N_e$ corresponding to the three heights and those of d$h'F$ corresponding to the three frequencies are plotted by shifting 2 and 5 units, respectively. Spread $F$ was observed after the $E$ region sunset (shown as red arrow) and clearly before the $F$ region sunset (shown as black arrow). Note that just prior to the occurrence of spread $F$, $h'F$ was well above 350 km and $V_z$ was as high as 42 m s$^{-1}$. From Figures 2c and 2d, one could notice wave-like variations with downward phase progression in both electron density and height variations. While the wave-like variations are found to be more predominant in electron density variations than those in the height variations, it is interesting to note the relationship between the two parameters during 15:00–16:30 local time (LT): Low (high) values of electron density perturbations are associated with high (low) values of height perturbations both following similar downward phase progression. After 17:00 LT, however, similar features are not present despite the fact that electron density perturbations show wave-like features with equal or stronger amplitude. This aspect needs additional investigation. The vertical wavelength ($\lambda_v$) and the corresponding horizontal wavelength ($\lambda_x$) of the gravity wave-like variations obtained using Equations 1 and 2 are 210 and 520 km, respectively. Figures 2e–2f show GIRI observations made on the same night displaying height-time variations of echo SNR including the plume structures that indicate occurrence of EPB, and east-west distribution and progression of EPB, respectively. One can notice four EPBs occurring overhead, and the first bubble occurred around 20:00 LT. The east-west separation between the first two bubbles, marked as pink thick line in Figure 2f, is estimated to be 550 km. Recall that the horizontal wavelength of gravity wave-like variations estimated using digisonde data is 520 km, and this estimate is based on the assumption of zero neutral wind. Thus, the horizontal wavelength of gravity wave-like variations and interbubble spacing are found to be in the comparable range.

In order to examine whether the correspondence between estimated wavelength and interbubble spacing is alike in all the data considered here, we have carried out similar exercise for all the 49 cases, and the results are shown in Figure 3 as scatterplot of horizontal wavelength of wave-like variations and interbubble spacing. It may be mentioned that the interbubble spacings have been estimated from the first two/three bubbles to avoid uncertainty due to fizzling out/decay of the subsequent bubbles. We noted that this approach is reasonable and there was no/negligible variation in interbubble spacing. The interbubble spacings estimated using GIRI observations are in the range of 200–550 km, and the horizontal wavelength estimated using digisonde observations are in the range of 160–520 km. Note that all the points in the scatterplot are aligned along the diagonal line, indicating connection between the two parameters. This result is quite encouraging despite the fact that we have assumed zero background neutral wind, which is certainly not a realistic scenario. In order to have some idea about the probable neutral wind values that might have caused the disagreement between the two parameters, we forced every value of horizontal wavelength to be equal to its corresponding interbubble spacing and estimated the neutral wind. The estimated neutral wind values are in the range of −40 to 70 m s$^{-1}$, which are quite realistic (e.g., Martinis et al., 2001; Meriwether et al., 2011; Raghavarao et al., 1998).

### 3.2. Role of Background Ionospheric Conditions

Although we have found reasonably good relation between the horizontal wavelength of the wave-like variations from digisonde observations and interbubble spacing from GIRI observations, implying that the wave-like variations could be potentially used as precursor seed of EPB, we have also found a few cases where the formation of EPB seemingly depends on background ionospheric conditions. To elucidate this scenario, we present two case studies in Figures 4 and 5.

Figure 4 shows the results based on observations made on 6 February 2015. Digisonde observations, presented in Figures 4a–4d, show that at the time of $F$ region sunset, $h'F$ was at 385 km and $V_z$ was limited to 20 m s$^{-1}$. Figures 4c and 4d clearly show wave-like variations with downward phase progression in both d$N_e$ and d$h'F$. Note that the wave-like variations have amplitudes comparable to or better than those

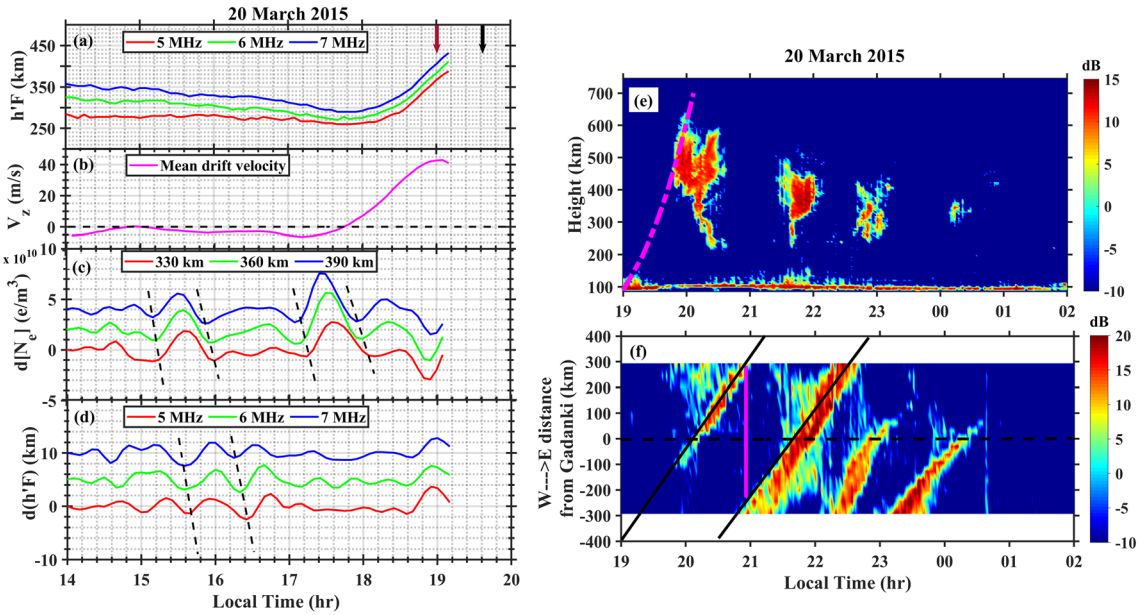


**Figure 2.** Temporal variations of (a) virtual height of the botomside *F* region ($h'F$) at 5, 6, and 7 MHz; (b) vertical plasma drift ($V_z$), (c) residual electron density ($dN_e$) at 330, 360, and 390 km, and (d) residual virtual height ($dh'F$) at 5, 6, and 7 MHz observed by digisonde on 20 March 2015. (e) Height-time variations of echo SNR observed by the north bearing of the GIRI on 20 March 2015. (f) Zonal distribution of irregularities at 350 km presented in terms of echo SNR observed on 20 March 2015. Magenta thick line intersecting the slant lines represents interbubble spacing. The red and black arrows in panel (a) represent *E* (100 km) and *F* (350 km) region sunset times. The slant line in panel (e) represents sunset time.

observed on 20 March 2015 (Figure 2). Vertical wavelength ($\lambda_v$) and horizontal wavelength ($\lambda_x$) of these variations are estimated to be 140 and 298 km, respectively. GIRI observations made on 6 February 2015, presented in Figure 4e, show no plume structure, indicating that no EPB occurred on this evening. Scanning observations (not shown) also did not reveal any plume. A bottomside echoing layer occurring around 250 km, however, was observed during 20:00–21:00 LT.

Figure 5 shows the results based on observations made on 26 March 2016. Digisonde observations, presented in Figures 5a–5d, show that at the time of *F* region sunset, $h'F$ was at 325 km and $V_z$ was limited to 16 m $s^{-1}$. Figures 5c and 5d clearly show wave-like variations with downward phase progression in both $dN_e$ and $dh'F$. Note that the wave-like variations have amplitudes comparable to or slightly higher at times than those observed on 6 February 2015. In this case, vertical wavelength ($\lambda_v$) and the horizontal wavelength ($\lambda_x$) of these variations are estimated to be 83 and 175 km, respectively. GIRI observations made on 26 March 2016 are presented in Figures 5e–5f in the same way as shown in Figure 2. Figure 5e shows periodic plume structures commencing from 19:45 LT. The east-west separation between the first two bubbles, marked as pink thick line in Figure 5f, is estimated to be 210 km.

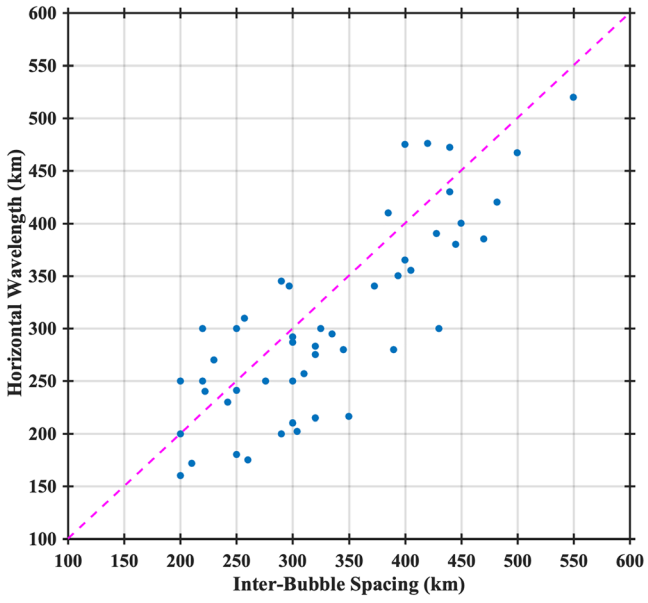


**Figure 3.** Scatterplot of horizontal wavelength of wave-like variations inferred from digisonde observations and interbubble spacing observed by the GIRI.

From results presented in Figures 4 and 5, we find that EPB occurred on 26 March 2016 but not on 6 February 2015 despite the fact that both $h'F$ and $V_z$ were lower on 26 March 2016 than those on 6 February 2015. Notably, on both days, wave structures of near-similar amplitudes were present. These indicate that other background conditions might have played decisive role in determing the growth of EPB. We found that the bottomside gradient scale length ($L$) during the sunset time on 6 February 2015 was 70 km, while it was only 40 km on 26 March 2016. Given that the bottomside gradient plays a crucial role, especially when the layer height is relatively

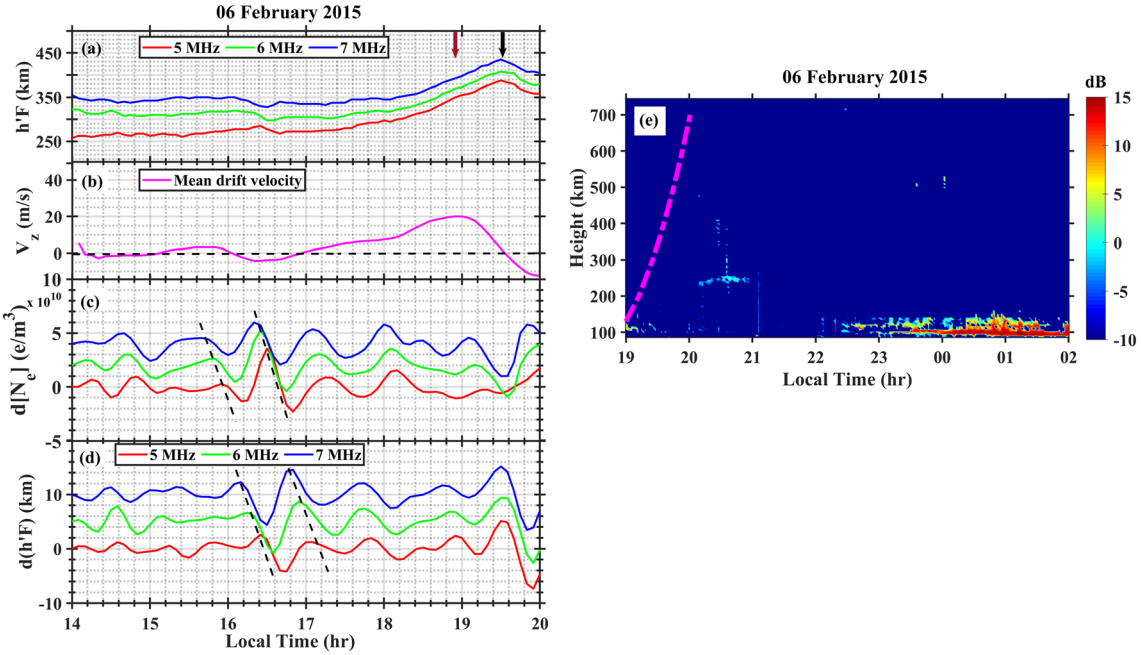


**Figure 4.** Same as Figure 2 except the zonal distribution of irregularities but for observations made on 6 February 2015.

low, we surmise that the gradient scale might have played the decisive role. We will discuss this aspect further in the following section while presenting simulation results.

## 4. Simulation Results

In order to assess the relative roles of seed wavelength and gradient scale length on the formation of EPB, we have carried out numerical simulation of the three-dimensional collisional interchange instability that includes $\mathbf{E} \times \mathbf{B}$ and RT instability mechansims (Kherani & Patra, 2015). The simulation code solves governing hydromagnetic equations for electron number density ($N$) and electrostaic potential ($\varphi$) numerically

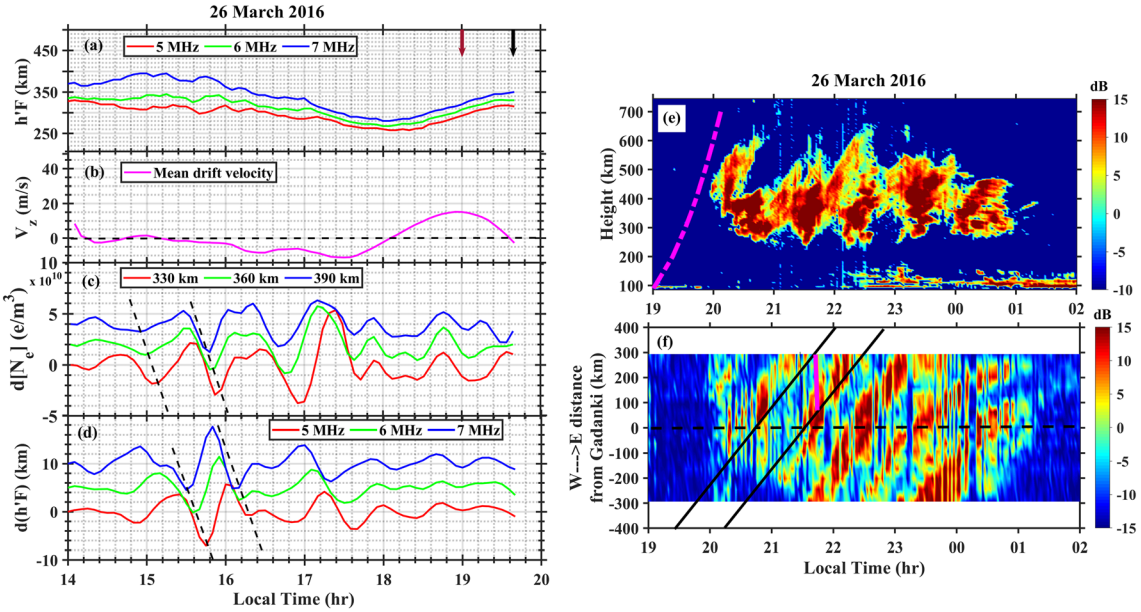


**Figure 5.** Same as Figure 2 but for observations made on 26 March 2016.

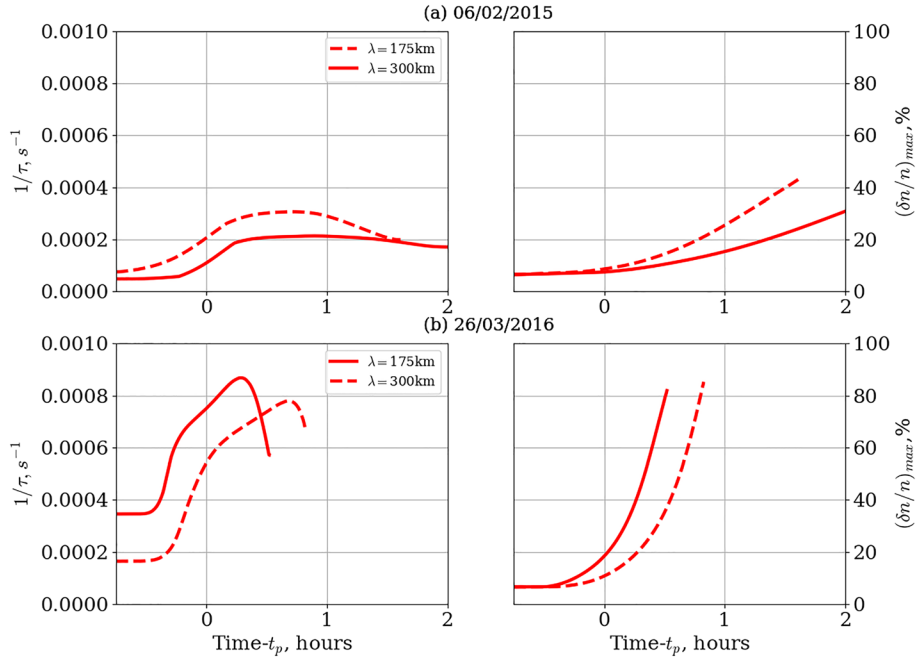


**Figure 6.** Growth rate of depletion ($1/\tau$) of collisional interchange instability (left column) and depletion level ($\delta N/N$) (right column) as a function of time corresponding to (a) 6 February 2015 and (b) 26 March 2016. Continuous lines represent results for observed wavelengths, and dashed lines represent results corresponding to interchanged wavelengths (i.e., 175 km instead of 300 km on 6 February and 300 km instead of 175 km on 26 March). The variable $t_p$ represents the time corresponding to peak vertical drift velocity on each day.

using finite difference method in three-dimensional simulation domain that consists of altitude, latitude, and longitude. The implicit Crank-Nicholson scheme is employed to perform the time integration leading to a matrix equation that is subsequently solved by the successive-over-relaxation method. The spherical polar coordinate system ($r$, $\theta$, $\phi$) is adopted, which represent the coordinates outward normal to the Earth's magnetic field, geomagnetic latitude (positive toward north), and longitude (positive toward west), respectively. The simulation domain consists of 90–890 km in altitude, ±20° in geomagnetic latitude, and ±3° in longitude. In the present study, we use electron densities and potentials obtained through numerical simulations under different background conditions. We also use the depletion level ($\delta N/N$) and the time rate of change of depletion level (hereafter referred to as growth rate of depletion). The depletion level is defined as $\delta N/N = (N_{in} - N_{out})/N_{out}$, where $N_{in}$ and $N_{out}$ represent the value of ($N$) inside and outside a depletion, respectively. The growth rate of depletion ($1/\tau$) is defined as $1/\tau = \mathrm{d}/\mathrm{d}t\,(\delta N/N)$. We have estimated the rate of change of depletion level ($1/\tau$) from simulation output.

To assess the competing roles of density gradient and seed wavelength in the formation of EPB, we have considered the observational parameters, namely, the $F$ layer height, vertical drift ($V_z$), gradient scale height ($H$), and seeding wavelength ($\lambda_x$) observed on 6 February 2015 and 26 March 2016 (presented in Figures 4 and 5). The initial seeding amplitude used in the simulation was kept at 5% for both the cases. We have also evaluated the relative role of seed wavelength on the bubble development keeping the background ionospheric parameters unchanged. For this purpose, we have carried out two simulation experiments: SE-1, where we have used the observed wavelengths, and SE-2, where we have interchanged the wavelengths. It may be recalled that observed horizontal wavelengths are 300 km on 6 February 2015 and 175 km on 26 March 2016. The simulation results are presented in Figures 6 and 7.

Figures 6a and 6b show growth rate of depletion ($1/\tau$) and depletion level ($\delta N/N$) as a function of time corresponding to 6 February 2015 and 26 March 2016, respectively. It may be mentioned that $\delta N/N$ represents its maximum value found in the altitude range of 300–550 km and at the center of the depletion. Solid lines represent results for observed wavelengths, and the dashed lines represent results corresponding to interchanged wavelengths, that is, 175 km instead of 300 km on 6 February 2015 and 300 km instead of

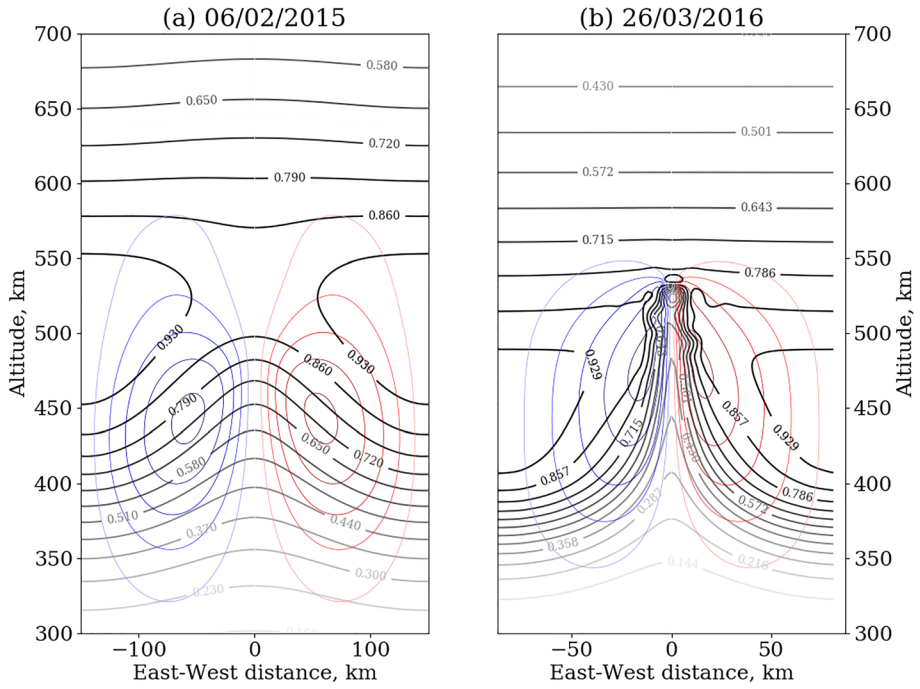


**Figure 7.** Isodensity contours of electron density with observed ambient and seeding conditions on (a) 6 February 2015 and (b) 26 March 2016. The background red and blue contours represent positive and negative potentials, respectively.

175 km on 26 March 2016. Rest of the parameters have been kept unchanged. For the observed wavlengths (solid lines), it is evident that while on 6 February the depletion level ($\delta N/N$) attained only 30% in 2 hr, on 26 March 2016, it attained more than 80% just in half an hour. The growth rates of depletion ($1/\tau$) also reflect this contrast in terms of nearly five times slower growth rate on 6 February 2015 than on 26 March 2016. These results suggest that the initial depletion of 5% could grow into EPB on 26 March 2016 but not on 6 February 2015. Coming to the simulation results with the wavelengths interchanged, which are depicted by dashed lines, shows that on 6 February 2015, depletion level ($\delta N/N$) attained ~40% in 1.5 hr and on 26 March 2016 it took 45 min to attain 80%. The growth rates of depletion ($1/\tau$) also reflect corresponding changes, that is, growth rate slightly increased on 6 February 2015 and decreased on 26 March 2016. Still, the depletion levels and growth rates of depletion on 6 February 2015 for both seed wavelengths are remarkably lower than those on 26 March 2016.

Figures 7a and 7b show simulation outputs obtained using the observed ambient and seeding conditions for 6 February 2015 and 26 March 2016, respectively. The isodensity contours of electron density show clear uplift of the low-density bottomside plasma into the topside through the depleted region on 26 March 2016, which is missing on 6 February 2015. Conspicuously, the penetration of the depleted region on 26 March 2016 is quite consistent with the height extension of the plume structures in the GIRI observations (shown in Figure 5).

We also performed an extra simulation for the case of 6 February 2015 by reducing the wavelength to 100 km (results not shown). We found that while the growth rate of depletion increased considerably and depletion in plasma density was noted, the depleted channel did not penetrate into the topside of the *F* region. This indicates that while the shorter wavelength provided better growth perspective of EPB, reducing the wavelength below a threshold did not result in sufficient depletion penetrating into the topside and resulting in EPB.

## 5. Discussion and Concluding Remarks

Collocated GIRI and digisonde observations from Gadanki have been used for the first time to study the linkage between wave-like variations in plasma frequency reflection prior to the sunset and interbubble spacing.

Notably, we have used the scanning capability of the GIRI to infer interbubble spacing to relate them to the inferred horizontal wavelength of the wave-like variations in digisonde observations. The application of this approach is first of its kind, and the scanning capability of the GIRI truly helped us not only in characterizing the interbubble spacing but also in defining the onset time and location of EPB within the radar field of view encompassing about 1,000 km zonal space centered on Gadanki. We have also characterized the wave structures in electron density variations, which is an addition to the commonly used height variations for this purpose (e.g., Abdu et al., 2009). Remarkably, we have found conspicuous signature of wave structures in electron density variations, and these structures were also consistent with those observed in height variations.

The interbubble spacings are found to be in the range of 200–550 km, which very well agree with those commonly observed and reported in the literature (Fukao et al., 2006; Hysell et al., 2005; Hysell & Chau, 2006; Kelley et al., 1981; Makela et al., 2010; Röttger, 1973; Singh et al., 1997; Takahashi et al., 2009; Tsunoda, 1983; Tsunoda & White, 1981). We have found a fairly good agreement between the inferred horizontal wavelength and the interbubble spacing despite the fact that horizontal wavelengths were inferred with zero neutral wind. This is a remarkable result and supports the basic idea proposed by Abdu et al. (2009) that digisonde observations of plasma frequency reflection prior to the sunset could be used in studying wave-like variations in the ionosphere with potential application for the prediction of EPB. With regard to interbubble spacings and their linkage to gravity waves, Makela and Otsuka (2012) have reviewed all earlier observations and found that while the observed interbubble spacings were shown to agree with the observed horizontal wavelengths of gravity waves in the thermosphere, they were not based on simultaneous observations and were also not from same location, presumably due to lack of coordinated measurements. Makela and Otsuka (2012) also discussed a few studies, which used airglow imager observations of the mesospheric gravity waves (using OH emission) and ionospheric plasma depletion (using OI 630-nm emission) made simultaneously, and found good relationship between horizontal wavelength of gravity waves and interbubble spacing (e.g., Takahashi et al., 2009; Taori et al., 2010). While these observations are remarkable in understanding the linkage between gravity waves and EPB, they lacked observational evidence of gravity waves in the thermosphere (ionospheric *F* region) to be more conclusive. From this perspective, the present observations assume significance, and we envisage that coordinated measurements using airglow imagers, radar, and modern digisonde may shed more light in understanding the linkage between gravity waves and EPB.

Having found that generally there is a fairly good agreement between the inferred horizontal wavelength and interbubble spacing, we have also observed some differences in detail between the two on a case-by-case basis. The difference can be attributed to the assumption of zero neutral wind and the experimental technique used. When the inferred horizontal wavelength is enforced to be equal to the interbubble spacing, the required wind magnitude was found to be well within the observed limits (Martinis et al., 2001; Meriwether et al., 2011; Raghavarao et al., 1998). The neutral wind, which is important for characterizing the waves in terms of their vertical and horizontal wavelengths, however, would continue to be an issue owing to lack of observational technique to measure it prior to sunset. The other aspect is the assumption that the observed wave structures in digisonde observations are east-west oriented, which may not be realistic. This issue can be addressed with the modern digisondes, which are equipped with interferometry. This may, however, require additional attention while conducting experiments to characterize the wave structures in question, a task to be taken up in a future study. Since the inferred horizontal wavelengths are in broad agreement with the interbubble spacing, we surmise that fixing the orientation of the wave structures by interferometry could greatly account for the observed difference. To that extent, digisonde observations could be suitably used to infer seed structures in question for its eventual application for EPB forecasting.

With regard to the role of bottomside *F* layer height and the density gradient scale length, we have demonstrated the critical role of density gradient scale length in the formation of EPB. Observational results, shown in Figures 4 and 5, indicated the importance of the gradient scale length (40 km) in forming the EPB on 26 March 2016 despite the height of the *F* layer being low (325 km), but not on 6 February 2015. Simulation results clearly underlined the importance of gradient scale length on the growth of EPB. Simulation results also demonstrated the seed wavelength dependence of the growth rate, consistent with the seeding wavelength dependence of the EPB growth reported earlier by Huang and Kelley (1996c). It may be mentioned that Huang and Kelley (1996c) showed the growth of EPB to be inversely proportional to the seeding

wavelength of gravity wave origin. We have further found that while the shorter wavelength has better growth rate, reducing the wavelength below a threshold could not result in sufficient depletion penetrating into the topside and resulting in EPB. Based on the observational and simulation results, we surmise that small gradient scale length and low *F* layer height might have played an additional role in terms of reduced field line-integrated Pedersen conductivity in the RT instability growth rate. This aspect, however, needs further investigation.

In conclusion, we have shown a fairly good relationship between the wave-like variations prior to sunset and interbubble spacing. We have shown that the inferred wave parameters using digisonde observations could form a potential precursor of EPB if the modern digisondes, which are equipped with interferometry, are used aptly. We have also examined the roles of the height of the *F* layer and density gradient scale length vis-à-vis the seeding wavelength, providing additional insight on the development of EPB.

**Acknowledgments**
Authors gratefully thank NARL technical team for making the GIRI and digisonde observations. Observations and simulation data presented here can be accessed from NARL data center (https://www.narl.gov.in/pdc/B5A48BBEE). One of the authors (S. K. D.) thanks NARL for supporting his research through research fellowship.

## References

Abdu, M. A., de Souza, J. R., Kherani, E. A., Batista, I. S., MacDougall, J. W., & Sobral, J. H. A. (2015). Wave structure and polarization electric field development in the bottomside *F* layer leading to postsunset equatorial spread F. *Journal of Geophysical Research: Space Physics*, *120*, 6930–6940. https://doi.org/10.1002/2015JA021235

Abdu, M. A., Kherani, E. A., Batista, I. S., de Paula, E. R., Fritts, D. C., & Sobral, J. H. A. (2009). Gravity wave initiation of equatorial spread F/plasma bubble irregularities based on observational data from the SpreadFEx campaign. *Annales Geophysicae*, *27*(7), 2607–2622. https://doi.org/10.5194/angeo-27-2607-2009

Fritts, D. C., & Alexander, M. J. (2003). Gravity wave dynamics and effects in the middle atmosphere. *Reviews of Geophysics*, *41*(1), 1003. https://doi.org/10.1029/2001RG000106

Fukao, S., Yokoyama, T., Tayama, T., Yamamoto, M., Maruyama, T., & Saito, S. (2006). Eastward traverse of equatorial plasma plumes observed with the Equatorial Atmosphere radar in Indonesia. *Annales Geophysicae*, *24*(5), 1411–1418. https://doi.org/10.5194/angeo-24-1411-2006

Huang, C. -S., & Hairston, M. R. (2015). The postsunset vertical plasma drift and its effects on the generation of equatorial plasma bubbles observed by the C/NOFS satellite. *Journal of Geophysical Research: Space Physics*, *120*, 2263–2275. https://doi.org/10.1002/2014JA020735

Huang, C. -S., & Kelley, M. C. (1996a). Nonlinear evolution of equatorial spread *F*: 1. On the role of plasma instabilities and spatial resonance associated with gravity wave seeding. *Journal of Geophysical Research*, *101*(A1), 283–292. https://doi.org/10.1029/95JA02211

Huang, C. -S., & Kelley, M. C. (1996b). Nonlinear evolution of equatorial spread *F*: 2. Gravity wave seeding of Rayleigh-Taylor instability. *Journal of Geophysical Research*, *101*(A1), 293–302. https://doi.org/10.1029/95JA02210

Huang, C. -S., & Kelley, M. C. (1996c). Nonlinear evolution of equatorial spread *F*: 4. Gravity waves, velocity shear, and day-to-day variability. *Journal of Geophysical Research*, *101*(A11), 24,521–24,532. https://doi.org/10.1029/96JA02332

Hysell, D. L., & Chau, J. L. (2006). Optimal aperture synthesis radar imaging. *Radio Science*, *41*, RS2003. https://doi.org/10.1029/2005RS003383

Hysell, D. L., Kelley, M. C., Swartz, W. E., & Woodman, R. F. (1990). Seeding and layering of equatorial spread *F* by gravity waves. *Journal of Geophysical Research*, *95*(A10), 17,253–17,260. https://doi.org/10.1029/JA095iA10p17253

Hysell, D. L., & Kudeki, E. (2004). Collisional shear instability in the equatorial *F* region ionosphere. *Journal of Geophysical Research*, *109*, A11301. https://doi.org/10.1029/2004JA010636

Hysell, D. L., Larsen, M. F., Swenson, C. M., Barjatya, A., Wheeler, T. F., Sarango, M. F., et al. (2005). Onset conditions for equatorial spread F determined during EQUIS II. *Geophysical Research Letters*, *32*, L24104. https://doi.org/10.1029/2005GL024743

Kelley, M. C. (1985). Equatorial spread *F*: Recent results and outstanding problems. *Journal of Atmospheric and Terrestrial Physics*, *47*(8-10), 745–752. https://doi.org/10.1016/0021-9169(85)90051-0

Kelley, M. C., Larsen, M. F., LaHoz, C., & McClure, J. P. (1981). Gravity wave initiation of equatorial spread *F*: A case study. *Journal of Geophysical Research*, *86*(A11), 9087–9100. https://doi.org/10.1029/JA086iA11p09087

Kherani, E. A., & Patra, A. K. (2015). Fringe field dynamics over equatorial and low latitude ionosphere: A three dimensional perspective. *Journal of Geophysical Research: Space Physics*, *120*, 6941–6947. https://doi.org/10.1002/2015JA021438

Kil, H., Oh, S.-J., Paxton, L. J., & Fang, T.-W. (2009). High-resolution vertical E × B drift model derived from ROCSAT-1 data. *Journal of Geophysical Research*, *114*, A10314. https://doi.org/10.1029/2009JA014324

Kudeki, E., Akgiray, A., Milla, M., Chau, J. L., & Hysell, D. L. (2007). Equatorial spread-F initiation: Post-sunset vortex, thermospheric winds, gravity waves. *Journal of Atmospheric and Solar-Terrestrial Physics*, *69*(17-18), 2416–2427. https://doi.org/10.1016/j.jastp.2007.04.012

Makela, J. J., & Otsuka, Y. (2012). Overview of nighttime ionospheric instabilities at low- and mid-latitudes: Coupling aspects resulting in structuring at the mesoscale. *Space Science Reviews*, *168*(1-4), 419–440. https://doi.org/10.1007/s11214-011-9816-6

Makela, J. J., Vadas, S. L., Muryanto, R., Duly, T., & Crowley, G. (2010). Periodic spacing between consecutive equatorial plasma bubbles. *Geophysical Research Letters*, *37*, L14103. https://doi.org/10.1029/2010GL043968

Martinis, C., Meriwether, J., Niciejewski, R., Biondi, M., Fesen, C., & Mendillo, M. (2001). Zonal neutral winds at equatorial and low latitudes. *Journal of Atmospheric and Solar-Terrestrial Physics*, *63*(14), 1559–1569. https://doi.org/10.1016/S1364-6826(01)00022-0

Meriwether, J. W., Makela, J. J., Huang, Y., Fisher, D. L., Buriti, R. A., Medeiros, A. F., & Takahashi, H. (2011). Climatology of the nighttime equatorial thermospheric winds and temperatures over Brazil near solar minimum. *Journal of Geophysical Research*, *116*, A04322. https://doi.org/10.1029/2011JA016477

Narayanan, V. L., Taori, A., Patra, A. K., Emperumal, K., & Gurubaran, S. (2012). On the importance of wave-like structures in the occurrence of equatorial plasma bubbles: A case study. *Journal of Geophysical Research*, *117*, A01306. https://doi.org/10.1029/2011JA017054

Patra, A. K., Srinivasulu, P., Chaitanya, P. P., Rao, M. D., & Jayaraman, A. (2014). First results on low-latitude *E* and *F* region irregularities obtained using the Gadanki Ionospheric Radar Interferometer. *Journal of Geophysical Research: Space Physics*, *119*, 10,276–10,293. https://doi.org/10.1002/2014JA020604

Patra, A. K., Taori, A., Chaitanya, P. P., & Sripathi, S. (2013). Direct detection of wavelike spatial structure at the bottom of the *F* region and its role on the formation of equatorial plasma bubble. *Journal of Geophysical Research: Space Physics*, *118*, 1196–1202. https://doi.org/10.1002/jgra.50148

Raghavarao, R., Suhasini, R., Hoegy, W. R., Mayr, H. G., & Wharton, W. (1998). Local time variation of equatorial temperature and zonal wind anomaly (ETWA). *Journal of Atmospheric and Solar-Terrestrial Physics*, *60*(6), 631–642. https://doi.org/10.1016/S1364-6826(97)00130-2

Röttger, J. (1973). Wave-like structures of large-scale equatorial spread-*F* irregularities. *Journal of Atmospheric and Solar-Terrestrial Physics*, *35*(6), 1195–1206. https://doi.org/10.1016/0021-9169(73)90016-0

Singh, S., Johnson, F. S., & Power, R. A. (1997). Gravity wave seeding of equatorial plasma bubbles. *Journal of Geophysical Research*, *102*(A4), 7399–7410. https://doi.org/10.1029/96JA03998

Smith, J. M., Rodrigues, F. S., Fejer, B. G., & Milla, M. A. (2016). Coherent and incoherent scatter radar study of the climatology and day-to-day variability of mean *F* region vertical drifts and equatorial spread *F*. *Journal of Geophysical Research: Space Physics*, *121*, 1466–1482. https://doi.org/10.1002/2015JA021934

Sreeja, V., Vineeth, C., Pant, T. K., Ravindran, S., Sridharan, R. (2009). Role of gravity wavelike seed perturbations on the triggering of ESF – a case study from unique dayglow observations. *Annales Geophysicae*, *27*(1), 313–318. http://doi.org/10.5194/angeo-27-313-2009

Su, S.-Y., Chao, C. K., & Liu, C. H. (2008). On monthly/seasonal/longitudinal variations of equatorial irregularity occurrences and their relationship with the postsunset vertical drift velocities. *Journal of Geophysical Research*, *113*, A05307. https://doi.org/10.1029/2007JA012809

Takahashi, H., Taylor, M. J., Pautet, P. -D., Medeiros, A. F., Gobbi, D., Wrasse, C. M., et al. (2009). Simultaneous observation of ionospheric plasma bubbles and mesospheric gravity waves during the SpreadFEx Campaign. *Annales Geophysicae*, *27*, 1477–1487. https://doi.org/10.5194/angeo-27-1477-2009

Taori, A., Makela, J. J., & Taylor, M. (2010). Mesospheric wave signatures and equatorial plasma bubbles: A case study. *Journal of Geophysical Research*, *115*, A06302. https://doi.org/10.1029/2009JA015088

Taori, A., Patra, A. K., & Joshi, L. M. (2011). Gravity wave seeding of equatorial plasma bubbles: An investigation with simultaneous *F* region, *E* region, and middle atmospheric measurements. *Journal of Geophysical Research*, *116*, A05310. https://doi.org/10.1029/2010JA016229

Tsunoda, R. T. (1983). On the generation and growth of equatorial backscatter plumes. 2. Structuring of the west walls of upwellings. *Journal of Geophysical Research*, *88*(A6), 4869–4874. https://doi.org/10.1029/JA088iA06p04869

Tsunoda, R. T., & White, B. R. (1981). On the generation and growth of equatorial backscatter plumes: 1. Wave structure in the bottomside *F* layer. *Journal of Geophysical Research*, *86*, 3610–3616. https://doi.org/10.1029/JA086iA05p03610

Woodman, R. F., Chau, J. L., & Ilma, R. R. (2006). Comparison of ionosonde and incoherent scatter drift measurements at the magnetic equator. *Geophysical Research Letters*, *33*, L01103. https://doi.org/10.1029/2005GL023692